X-Rays from Superbubbles in the Large Magellanic Cloud. VI. A Sample of Thirteen Superbubbles

Bryan C. Dunne, Sean D. Points, and You-Hua Chu

Department of Astronomy, University of Illinois, 1002 West Green Street, Urbana, IL 61801

carolan@astro.uiuc.edu, points@astro.uiuc.edu, chu@astro.uiuc.edu

ABSTRACT

We present ROSAT observations and analysis of thirteen superbubbles in the Large Magellanic Cloud. Eleven of these observations have not been previously reported. We have studied the X-ray morphology of the superbubbles, and have extracted and analyzed their X-ray spectra. Diffuse X-ray emission is detected from each of these superbubbles, and X-ray emission is brighter than is theoretically expected for a wind-blown bubble, suggesting that the X-ray emission from the superbubbles has been enhanced by interactions between the superbubble shell and interior SNRs. We have also found significant positive correlations between the X-ray luminosity of a superbubble and its $H\alpha$ luminosity, expansion velocity, and OB star count. Further, we have found that a large fraction of the superbubbles in the sample show evidence of "breakout" regions, where hot X-ray emitting gas extends beyond the $H\alpha$ shell.

Subject headings: ISM: bubbles, galaxies: individual (LMC)

1. Introduction

Superbubbles are large (\sim 100 pc across) shells in the interstellar medium (ISM) created by the combined action of stellar winds and supernova explosions of massive stars in an OB association. The hot (\gtrsim 10⁶ K) shock-heated gas interior to superbubbles emits X-ray radiation. X-ray observations of superbubbles can reveal a wealth of information on the structure and interior of superbubbles. An excess of diffuse X-ray emission in superbubbles can indicate the presence of interior supernova remnants (SNRs) shocking the inner walls of the superbubble shell (Chu & Mac Low 1990, hereafter Paper I; Wang & Helfand 1991). The diffuse X-ray emission can also be used to find "breakout" regions where the hot gas

from the superbubble interior may be leaking out into the ISM. Unresolved peaks superposed on the diffuse X-ray emission may also indicate the presence of stellar X-ray sources interior to the superbubble.

The Large Magellanic Cloud (LMC) provides an ideal laboratory for observing superbubbles in the X-ray spectrum. The coverage of Galactic superbubbles is far from complete because of extinction from the disk of the Milky Way. Non-Magellanic Cloud extragalactic superbubbles are too far away to be angularly resolved by X-ray instruments such as ROSAT. The LMC, however, provides a sample in excess of 20 superbubbles, at a common distance (\sim 50 kpc, Feast 1999), that are resolvable by modern X-ray detectors. Observations of the superbubbles in the LMC can provide us with great insight into the interaction among superbubbles, SNRs, and the ISM.

We have been studying X-ray emission from superbubbles in the LMC. In Paper I, Einstein observations were used to show that seven LMC superbubbles are diffuse X-ray sources with luminosities much higher than those expected by the wind-blown, pressure-driven bubble models of Weaver et al. (1977). Off-center SNRs are proposed to be responsible for the excess X-ray emission. ROSAT observations of the superbubble N44 confirmed its diffuse X-ray emission and provided the first useful X-ray spectra of N44 for determinations of plasma temperatures (Chu et al. 1993, hereafter Paper II). To illustrate that excess X-ray emission from superbubbles is caused by an intermittent process, Chu et al. (1995, hereafter Paper III) analyzed ROSAT observations of four X-ray-dim superbubbles, and showed that these superbubbles do not have excess X-ray emission. For high-resolution spectral analysis, ASCA observations of N44 were made; the ASCA data showed that the hot gas in the breakout region is slightly cooler than that in the superbubble interior (Magnier et al. 1996, hereafter Paper IV). ROSAT observations of the H II complex N11 were analyzed to study the interaction between OB associations, H II regions, and superbubbles (Mac Low et al. 1998, hereafter Paper V).

In this latest study, we have analyzed ROSAT observations of eleven H α -indentified superbubbles in the LMC whose observations had not been reported previously. Diffuse X-ray emission was detected in every one of these eleven superbubbles. We have re-analyzed N44 and N11 in order to have a homogeneous set of results for comparisons. We have modeled these superbubbles using the pressure-driven bubble models of Weaver et al. (1977). In this paper, we report the ROSAT observations of the thirteen superbubbles studied, and discuss the X-ray luminosities and other properties of the superbubbles and their relationship with the LMC.

2. X-Ray Dataset and Analysis

2.1. ROSAT Archival Dataset

Our dataset is based on a selection of known LMC superbubbles around OB associations with a well-defined H α morphology. We have further constrained the sample to include only those superbubbles with previously unreported ROSAT observations with at least 5 ks exposure. The superbubbles studied are in N51, N57, N103, N105, N144, N154, N158, N160, N206 (nomenclature of Henize 1956), and 30 Dor C. Two superbubbles are present in N51, making the total number of superbubbles eleven. For comparisons with previous results, we have also included N11 and N44 in the dataset. The coordinates, sizes, H α luminosities, expansion velocities, and local OB associations of this sample of thirteen superbubbles, as well as alternative designations, are summarized in Table 1.

Two detectors are available on board the ROSAT satellite: the Position-Sensitive Proportional Counter (PSPC) and the High-Resolution Imager (HRI). We have used PSPC observations to investigate physical conditions and distribution of the 10^6 K gas interior to most of the LMC superbubbles in our dataset. The PSPC is sensitive to X-ray photons with energies in the range of 0.1-2.4 keV and has an energy spectral resolution of $\sim 40\%$ at 1 keV, with a field of view of $\sim 2^\circ$. As the HRI is better suited to revealing points sources rather than diffuse emission, we have used HRI observations to investigate the distribution of X-ray emitting gas only in the superbubble N206, which fell close to the outer edge of the field-of-view in the PSPC observations. The HRI is sensitive in the energy range of 0.1-2.0 keV, with a field of view of $\sim 40'$. Further information on the PSPC and HRI can be found in Pfefferman et al. (1987) and the ROSAT Mission Description (1991). A summary of the individual observations can be found in Table 2.

2.2. X-Ray Data Analysis

We have studied both the X-ray morphology and X-ray spectra of the superbubbles in the dataset. All of the data were reduced using standard routines in IRAF¹ and the PROS² package.

¹Image Analysis and Reduction Facility – IRAF is distributed by the National Optical Astronomy Observatories, which are operated by the Association of Universities for Research in Astronomy, Inc., under cooperative agreement with the National Science Foundation.

²PROS/XRAY Data Analysis System – http://hea-www.harvard.edu/PROS/pros.html

2.2.1. Morphology

Analysis of the X-ray morphology of each superbubble was conducted using smoothed PSPC and HRI images. The images were binned to 4" pixels and then smoothed with Gaussian function of $\sigma=4$ pixels. We have compared the X-ray morphologies with the H α morphologies observed in the PDS scans of the Curtis Schmidt plates of Kennicutt & Hodge (1986). In Figure 1, we present the H α images overlaid with X-ray contours. We also present the X-ray images overlaid with the same contours to ensure the clarity of the contour levels. The contours are at levels of 50%, 70%, 85%, and 95% of the peak level within the superbubble. For bright X-ray objects in the field not actually part of the superbubble (such as SNRs), we have plotted additional contours at 2, 4, 8, and 16 times the superbubble peak level. These contours are plotted as dashed lines.

2.2.2. Spectral Fits

The X-ray spectra of the superbubbles were extracted from the PSPC data. We defined source regions for each superbubble. Then, possible stellar sources (i.e., X-ray binaries, Wolf-Rayet stars) were excised from the data before the spectra were extracted. Additionally, we selected several background regions around each superbubble (This is especially important for superbubbles superposed on large extended LMC sources of diffuse X-ray emission, such as the 30 Doradus complex and the supergiant shells LMC2 and LMC3). The background-subtracted spectra were then extracted from the PSPC event files.

The observed X-ray spectrum of each superbubble is a convolution of several factors: the intrinsic X-ray spectrum of the superbubble, the intervening interstellar absorption, and the PSPC response function. Because the interstellar absorption and the PSPC response function are dependent on photon energy, we must assume models of the intrinsic X-ray spectrum and the interstellar absorption to make the problem tractable. As the X-ray emission from the superbubble interiors appears largely diffuse, we have used the Raymond & Smith (1977) thin-plasma emission model and the Morrison & McCammon (1983) effective absorption cross-section per hydrogen atom to describe the intrinsic X-ray spectra of the superbubbles and the foreground absorption, respectively. We then simulate the observed spectrum, combining the assumed models for the intrinsic spectrum and the interstellar absorption with the response function of the PSPC. The observed spectrum is fitted with the simulated spectra; the χ^2 of the fits determines the best-fit.

We performed a χ^2 grid search of simulated spectral fits to determine the best-fit levels for the temperature, kT, and absorption column density, $N_{\rm H}$. From these model fits, we can

calculate the un-absorbed X-ray flux, and therefore the X-ray luminosity, $L_{\rm X}$, of the diffuse X-ray emission from the superbubbles. The normalization factor of the best fit can be used to determine the volume emission measure, adopting a distance of 50 kpc for the LMC (Feast 1999). If we assume a uniform density in the X-ray-emitting gas, the volume emission measure can be expressed as $N_{\rm e}^2 f V$, where $N_{\rm e}$ is the electron density, f is the volume filling factor, and V is the volume of the superbubble interior. Assuming the superbubbles have an ellipsoidal shape, we can use the observed diameters of the superbubbles to determine $N_{\rm e} \sqrt{f}$. The net exposure time, background-subtracted source counts, scaled background counts, and best-fit values of kT, $N_{\rm H}$, $L_{\rm X}$ and $N_{\rm e} \sqrt{f}$ for a 30% solar abundance Raymond & Smith (1977) thermal plasma model are given in Table 3. Plots of the fits to the superbubbles' X-ray spectra are shown in Figure 2.

We have also sought to further constrain the models by using observations of the H I column density to independently determine the total absorption column density, $N_{\rm H}$. We have divided the absorption column into Galactic and LMC components and determined each separately. Arabadjis & Bregman (1999) demonstrated that in the X-ray spectrum, at Galactic latitudes $|b| > 25^{\circ}$, the contribution of molecular gas to the total absorption column density is comparable to the contribution of the neutral hydrogen gas. We have therefore approximated the Galactic absorption column density by $N_{\rm H} \simeq 2 \times N_{\rm HI}$. Continuing this approximation to the LMC absorption column density is more complicated. Measurements of LMC H I column density can sample material both in front of and behind a feature such as a superbubble. We have used the simplifying assumption that half of the LMC H I gas is foreground to the superbubbles and half is background. Thus, the LMC component of the total absorption column density is $\frac{1}{2} \times 2 \times N_{\rm HI} = N_{\rm HI}$. The total absorption column density is therefore given by $N_{\rm H} = 2 \times (N_{\rm HI})_{\rm Galactic} + (N_{\rm HI})_{\rm LMC}$.

We have used the observations of Galactic and LMC H I column densities by Dickey & Lockman (1990) and Rohlfs et al. (1984) to determine the total absorption column density. These calculated values of $N_{\rm H}$ are, on average, nearly an order of magnitude larger than values of $N_{\rm H}$ determined by the best-fit models to the X-ray spectra (see Table 4). Indeed, several of the Galactic $N_{\rm H}$ values are alone larger than those derived from the best-fit models. The calculated values of $N_{\rm H}$ also show a much narrower range of absorption column densities to the LMC superbubbles (log $N_{\rm H} = 21.3-21.7$) than the values of $N_{\rm H}$ derived from the best-fit models to the X-ray spectra (log $N_{\rm H} = 20.4-22.0$).

We have re-determined best-fit values for kT, $L_{\rm X}$, and N_e based again on a 30% solar abundance Raymond & Smith (1977) thermal plasma model, but with $N_{\rm H}$ fixed at the calculated values determined above. A summary of the results are given in Table 4. Plots of these "fixed $N_{\rm H}$ " fits to the superbubbles' X-ray spectra are shown in Figure 3.

3. Individual Superbubble Properties

We will now discuss each of the superbubbles studied individually. For each superbubble, although we primarily use the nomenclature of Henize (1956, e.g., N11), we give alternative designations as cataloged by Davies, Elliott, & Meaburn (1976, e.g., DEM L 192). We also give the OB associations and star clusters encompassed by the superbubble as reported in Lucke & Hodge (1970, e.g., LH63). General descriptions of the H α morphology, as seen in the PDS scans of the Curtis Schmidt plates of Kennicutt & Hodge (1986), and comparisons with X-ray morphology, from the smoothed PSPC images, are given. We also discuss breakout regions, possible identifications of X-ray hotspots with known stellar sources from Breysacher (1981, e.g., Br81) and Sanduleak (1969, e.g., Sk-66°28), and other interesting X-ray features. The linear sizes of the superbubbles are calculated assuming 1' = 15 pc.

3.1. N11-Shell 1

N11 (DEM L 34) is the second largest H II complex in the LMC (Kennicutt & Hodge 1986). N11 contains a superbubble 150 pc \times 100 pc in size, surrounded by several bright H α knots and smaller H α shells. The superbubble has been labeled Shell 1 in Paper V. Shell 1 encompasses the OB association LH 9. Diffuse X-ray emission is detected toward Shell 1 (See Figure 1a).

This diffuse X-ray is centrally bright and appears to be confined by the observed $H\alpha$ shell. The X-ray emission peaks at a location coincident with HD 32228, a known Wolf-Rayet star also cataloged as Br81 and Sk-66°28. Several smaller peaks are also evident in the diffuse X-ray emission. A more thorough interpretation of the X-ray emission can be found in Paper V.

3.2. N44 (DEM L 152)

N44 is a bright H II complex, similar to N11. N44 contains a superbubble, cataloged as DEM L 152, around the OB association LH 47. The 100 pc \times 75 pc superbubble is well-detected in H α emission with well-defined shell walls. Diffuse X-ray emission is detected toward DEM L 152 (See Figure 1b). Additionally, diffuse X-ray emission is detected \sim 6′ to the northeast of DEM L 152; this emission has been identified by Paper II as originating from a supernova remnant.

The diffuse X-ray emission correlates well with the H α shell of DEM L 152. The X-ray emission is limb-brightened, forming an X-ray shell just interior to the H α shell. A breakout region on the southern edge of the superbubble and an X-ray blister on the eastern edge of the shell are detected in the PSPC image as well. A more thorough interpretation of the X-ray emission and the breakout regions can be found in Paper II and Paper IV.

3.3. N51 (DEM L 192, DEM L 205)

N51 is a nebular complex encompassing five OB associations, LH 51, LH 54, LH 55, LH 60, and LH 63 (Paper I). Two ionized gas shells are visible in the H α image (see Figure 1c) and are cataloged as DEM L 192 and DEM L 205. DEM L 192 is the larger shell with a size of 135 pc \times 120 pc and contains the OB associations LH 51 and LH 54. DEM L 205 is the smaller shell with a size of 65 pc \times 50 pc. The morphology of DEM L 205 is that of a blister with the OB association LH 63 at the base. Diffuse X-ray emission is detected toward both of these optical shells.

The diffuse X-ray emission toward DEM L 192 is limb-brightened and confined within the optical H α shell. Therefore, it is reasonable to conclude that the X-ray emission is produced by hot gas interior to the superbubble. Additionally, an X-ray hotspot is detected within the superbubble and coincides with the Wolf-Rayet star Br31, also cataloged as Sk-67°104. Emission from this hotspot was excluded in the thermal plasma model fit of DEM L 192.

It is not clear whether the X-ray hotspot is a peak in the diffuse emission or a stellar source. Only 42±11 PSPC counts were detected from the hotspot. This count level is inadequate to constrain the three parameters upon which a thermal plasma emission model depends. Further high resolution X-ray observations are needed to explore the nature of this hotspot.

DEM L 205 also shows limb-brightening in the PSPC images. Unlike DEM L 192, no X-ray hotspots are detected within DEM L 205. On the southwestern side of this shell, where the H α surface brightness is lowest, the X-ray emission appears more extended than the main shell. X-ray emission of similar morphology is also detected in the Einstein observations of N51 (Paper I). This may indicate a breakout of the hot gas interior to DEM L 205 into a lower density region; however, the H α image hints at the presence of very faint outer H α filaments confining this emission.

3.4. N57 (DEM L 229)

N57 is a nebular complex encompassing the OB association LH 76. Two ionized gas shells are visible in the H α image (See Figure 1d) and are cataloged as DEM L 229 and DEM L 231. DEM L 229 is the larger shell; it is 200 pc × 100 pc in size and contains LH 76. The smaller shell, DEM L 231, 30 pc × 30 pc in size, is a ring nebula around the Wolf-Rayet star Br48 (Chu & Lasker 1980; Chu, Weis, & Garnet 1999). Of these two shells, diffuse X-ray emission is only detected toward DEM L 229. Additionally, a bright X-ray source is visible to the north of DEM L 229, the X-ray source is not associated with DEM L 229 and has been identified as the SNR candidate, SNR 0532-675 (Mathewson et al. 1985; Williams et al. 1999).

The diffuse X-ray emission toward DEM L 229 is coincident with the interior of the superbubble. The emission also appears to be largely confined by the optical $H\alpha$ shell. This indicates that the X-ray emission originates from the hot gas in the superbubble interior. The X-ray emission appears brightest towards the southern part of DEM L 229. Details of the X-ray morphology cannot be confidently determined, however, as N57 is detected on the outer edge of the PSPC (See Table 2) where the point-spread function becomes quite poor.

3.5. N103 (DEM L 84)

N103 is a nebular complex encompassing the star cluster NGC 1850. It has two main components, N103A (DEM L 85), the 20 pc × 15 pc H α knot on the east, and N103B³ (DEM L 84), a 120 pc × 120 pc superbubble on the west. Supernova remnant 0509–68.7 is present just exterior to the eastern edge of the superbubble (Mathewson et al. 1983; Williams et al. 1999), and the superbubble is brightest in H α on the eastern side closest to the SNR. Diffuse X-ray emission is detected toward both the superbubble and the supernova remnant (See Figure 1e).

The X-ray emission toward N103B appears to have several distinct structures. The most obvious is the very strong extended source that is coincident with the supernova remnant 0509-68.7. Another prominent structure is a large limb-brightened X-ray ring with a point X-ray source at the center. Chu et al. (2000) found that this X-ray ring is centered on the nearby star cluster HS122 (Hodge & Sexton 1966), which is projected at the southwest

 $^{^3}$ It should be noted here that the label "N103B" is often erroneously used to refer to the supernova remnant 0509-68.7. We are using "N103B" to refer to the H α structure as originally identified by Henize (1956).

rim of the superbubble. We therefore cannot assume that the majority of the diffuse X-ray emission detected toward N103B is caused by hot gas inside the superbubble of N103B. Further comparison of the X-ray and H α images presented in Figure 1e reveal diffuse X-ray emission in the region between the supernova remnant of N103B and the X-ray ring and coincident with the superbubble. Because of the PSPC's low scattering levels, it is reasonable to assume that this X-ray emission arises from hot gas within the superbubble. We have used this region as a sample of the X-ray emission from the superbubble of N103B.

3.6. N105 (DEM L 86)

N105 is a nebular region encompassing the OB association LH 31 (also cataloged as NGC 1858) and the star cluster NGC 1854. Two bright H α knots are visible as well as H α emission from the filaments of the 90 pc \times 60 pc superbubble shell. The larger H α knot is coincident with LH 31; the smaller knot is coincident with NGC 1854. Diffuse X-ray emission is detected toward the larger H α knot (See Figure 1f).

The strongest X-ray emission from N105 is coincident with LH 31, indicating that the X-ray emission is likely emitted by hot gas produced by the OB association. The diffuse X-ray is not confined by the H α emission of N105; instead, the emission extends eastward from N105 to a nearby patch of H α emission, DEM L 87. The diffuse X-ray emission appears to lose intensity approximately at the edge of DEM L 87. This suggests that the hot, X-ray emitting gas created by LH 31 is expanding eastward through a lower density medium to the denser gas in DEM L 87. At the interface with DEM L 87, the X-ray emission drops off, further suggesting interaction between the X-ray emitting gas of N105 and DEM L 87.

3.7. N144 (DEM L 199)

N144, encompassing the OB association LH 58, is a nebular region near the western rim of the supergiant shell LMC 3. A 120 pc \times 75 pc ionized gas shell is visible in the H α image (See Figure 1g). The morphology of N144 is a roughly circular complex made up of many blister-like bubbles surrounding a central shell structure. The central shell has the brightest H α emission of the nebula on its northern side. Diffuse X-ray emission is weakly detected toward several of the bubble regions, including the central bubble.

The X-ray emission is generally coincident with N144, and the strongest X-ray emission is toward the central shell seen in the H α image. This indicates that the X-ray emission is likely to originate from the hot gas in the superbubble interior. There are two peaks in the X-

ray emission from the central shell. These peaks are generally coincident with the Wolf-Rayet stars Br34 and Br32, also cataloged as Sk $-68^{\circ}82$ and Sk $-68^{\circ}80$, indicating probable sources for the peaks in the diffuse X-ray emission (Hail, Dunne, & Chu 2001). The X-ray emission extends beyond the H α emitting shell of the central bubble to the northeast and southwest. Each of these "wings" from central concentration has its own weaker concentration of X-ray emission. This suggests that multiple-bubble structures in the N144 region have interior hot diffuse gas. The southwest "wing" of the X-ray emission shows further extension beyond the H α shell of N144. This may indicate a breakout of the hot gas interior to N144 into a lower density region.

3.8. N154 (DEM L 246)

N154 is a nebular complex to the south of the 30 Doradus region. The superbubble encompasses the OB associations LH 81 and LH 87. The 180 pc \times 120 pc H α shell of the superbubble is an angular, almost-rhomboid shape, with the strongest H α emission coming from the northeast and southwest sides. Diffuse X-ray emission is detected toward N154 (see Figure 1h). A bright X-ray source to the southwest of N154 has been identified as SNR 0534-699 (Mathewson et al. 1983; Williams et al. 1999).

The diffuse X-ray toward N154 is centrally bright, and the morphology of the emission is that of an ellipsoidal running southwest to northeast - similar to the structure and size of the H α emission. It is reasonable to therefore assume that the diffuse X-ray emission arises from hot gas in the interior of the superbubble N154. There is significant X-ray emission trailing from N154 toward the northeast. Due to the strong X-ray background emission and number of X-ray sources near the 30 Doradus complex, it is difficult to determine if this emission trail is a breakout region of hot X-ray emitting gas from N154 or a blending of X-ray emission from N154 with emission from neighboring regions.

3.9. N158 (DEM L 269)

N158 is a complex nebular structure to the south of the 30 Doradus. The complex encompasses the OB associations LH 101 and LH 104. The superbubble is located on the northern part of the N158 complex and has a well-defined, 100 pc \times 90 pc shell in the H α . Diffuse X-ray emission is detected toward N158 (See Figure 1i). Two strong X-ray sources are detected to the north and west, respectively, of N158 as well. The source north of N158 appears to be coincident with the known SNR and pulsar PSR B0540-69.3 (Mathewson et

al. 1983; Bica et al. 1998), and the position of the source west of N158 is consistent with the Einstein X-ray source 0538.5-6925, a foreground Galactic star (Cowley et al. 1997).

The diffuse X-ray emission toward N158 appears to be coincident with the superbubble. Although the X-ray emission is not confined by the observed H α shell, the morphology of the X-ray emission suggests that the emission is associated with N158, but that several breakout regions have formed along the shell where hot, X-ray emitting gas is escaping the interior of the superbubble. It must be cautioned, however, that the X-ray morphology of this region is exceedingly complex.

3.10. N160 (DEM L 284)

The nebular complex N160 is located on the southern side of the 30 Doradus region. The superbubble in N160 dominates the morphology of the complex. The superbubble is $180 \text{ pc} \times 150 \text{ pc}$ in size, and encompasses the OB association LH 103. The H α morphology is roughly circular, with a possible "blowout" region apparent on the northeast edge (Points et al. 1999). The H α emission is strongest on the southern edge of the superbubble, closest to LH 103. Diffuse X-ray emission is detected toward the superbubble (See Figure 1j). Additionally, there is a pair of strong X-ray sources south of N160. These sources have been identified: the brighter source is the X-ray binary LMC X-1 and the dimmer source is SNR 0540-697 (Chu et al. 1997; Williams et al. 2000).

The diffuse X-ray emission detected toward the superbubble in N160 is concentrated near LH 103. Little significant emission is detected from the remainder of the superbubble. This suggests that the stars and/or supernovae in LH 103 are producing hot X-ray emitting gas. The gas interior to the superbubble may be too hot to be detected in the PSPC energy bandpass, or the majority of the hot gas may simply have already escaped.

3.11. N206 (DEM L 221)

N206 (also cataloged as DEM L 221) is a nebular complex encompassing the OB associations LH 66 and LH 69. N206 contains both a superbubble and a smaller supernova remnant, SNR 532-710 (Mathewson et al. 1983; Williams et al. 1999). The 30 pc \times 30 pc remnant is located on the eastern side of the nebular complex, and has a faint circular H α shell. The superbubble has a larger circular shell, 110 pc \times 110 pc, with the brightest H α emission coming from the eastern and southern sides of the bubble. Diffuse X-ray emission is detected toward both the remnant and the superbubble (See Figure 1k). The diffuse X-ray

emission detected toward the supernova remnant has been previously explored by Williams et al. (1999).

The diffuse X-ray emission toward the superbubble of N206 appears to have a several enhancements, possibly in a limb-brightened ring. The emission is coincident with a region of the superbubble that is not bright in $H\alpha$, but the diffuse X-ray emission appears confined by faint $H\alpha$ structures on the western side of the superbubble. Therefore, it is reasonable to conclude that the X-ray emission is produced by hot gas interior to the superbubble.

One of the enhancements of the diffuse X-ray emission is coincident with the Wolf-Rayet star Br44. The X-ray emission from this enhancement in the superbubble may therefore have a stellar source rather than a diffuse one. The emission from this enhancement has therefore been excluded from the thermal plasma model fit of the superbubble in N206.

3.12. 30 Dor C (DEM L 263)

30 Dor C is a superbubble located in the southwestern region of the 30 Doradus complex. The superbubble encompasses the OB association LH 90. The H α emission shows a strong shell structure, 100 pc \times 90 pc in size. Diffuse X-ray emission is detected toward the superbubble (See Figure 11).

The X-ray emission detected toward 30 Dor C is limb-brightened and appears confined within the H α shell. It is therefore reasonable to conclude that the X-ray emission arises from within the superbubble. The limb-brightened shell is well-defined all around the superbubble except on the southwest, where the X-ray emission is near the background levels.

The absorption column density towards 30 Dor C is known to change dramatically across the face of the superbubble (Osterberg 1997). We have therefore divided 30 Dor C into two parts (east and west) to account for the change in absorption column density in our spectral fits. Unfortunately, the LMC $N_{\rm HI}$ maps from Rohlfs et al. (1984) do not have the spatial resolution to detect this change, so we must still use a single value in our "fixed $N_{\rm H}$ " fits of 30 Dor C.

4. Discussion

4.1. Distribution of X-ray Luminosities

Based on the spectral fits performed for each superbubble, we have computed X-ray luminosities. We have used these luminosities to investigate the superbubble luminosity function. In Figure 4, we present the X-ray luminosity function for the superbubbles in our dataset. We have plotted the luminosities as determined by both the "best-fit $N_{\rm H}$ " model fits and the "fixed $N_{\rm H}$ " model fits. The "best-fit $N_{\rm H}$ " luminosity function illustrates that most of the superbubbles in our sample have an X-ray luminosity around 10^{35-36} ergs sec⁻¹. A single high-end outlier is also shown at over 10^{37} ergs sec⁻¹; this outlier is N11–Shell 1. The "fixed $N_{\rm H}$ " luminosity distribution favors higher X-ray luminosities than the "best-fit $N_{\rm H}$ " luminosity distribution as well as a broader range in luminosities (excepting the outlier on the "best-fit $N_{\rm H}$ " luminosity function).

4.2. Pressure Driven Models

To compare the X-ray luminosities of the superbubbles derived from observation with the pressure-driven bubble models of Weaver et al. (1977) for the LMC superbubbles, we have followed the procedure described in Paper I and corrected in Paper III. Assuming that the shell thickness is small compared to the radius of the bubble, an electron temperature in the shell of $T_e \simeq 10^4$ K, and a mean atomic mass of the ambient medium $\mu_a = (14/11)m_{\rm H}$, we can use equations (7)–(10) from Paper III to derive the X-ray luminosity:

$$L_{\rm X} \simeq (6.7 \times 10^{29} {\rm erg \cdot sec^{-1}}) \cdot \xi \cdot I \cdot EM^{5/7} \cdot R_{\rm pc}^{12/7} \cdot v_{\rm exp}^{1/7}$$
 (1)

where ξ is the metallicity, assumed to be 0.3, I is a dimensionless function of the temperatures interior to the superbubble, which has a value \sim 2, EM is the emission measure of the 10^4 K shell gas in cm⁻⁶ pc, $R_{\rm pc}$ is the radius of the superbubble in parsecs, and $v_{\rm exp}$ is the superbubble expansion velocity in km sec⁻¹. The dimensions and expansion velocities of the superbubbles are given in Table 1. Unfortunately, we do not have expansion velocities for all of the superbubbles. The emission measure was determined from the continuum-subtracted H α image derived from the PDS scans of the Curtis-Schmidt plates of Kennicutt & Hodge (1986). The emission measures and theoretical X-ray luminosities are presented in Table 5. Of course, the emission measure can vary greatly around H α shell, so we have taken an rough mean for each superbubble. The predicted X-ray luminosities range from $10^{34.3}$ – $10^{35.1}$ erg sec⁻¹. These luminosities range from \sim 3 to \sim 50 times lower than the X-ray luminosities

determined from the PSPC data with the "fixed $N_{\rm H}$ " fits. This suggests that the majority of the X-rays are produced by different mechanisms than those described in the pressure-driven bubble model, confirming that the superbubbles in our sample are X-ray bright.

4.3. X-Ray Luminosity Correlations

We have also compared the superbubble volume, $H\alpha$ luminosity, expansion velocity, and bright star count with the X-ray luminosity, for both "best-fit $N_{\rm H}$ " and "fixed $N_{\rm H}$ " model fits (See Figures 5, 6, 7, & 8). The superbubble volumes were determined from the sizes of the H α shell (See Table 1), assuming an ellipsoidal shape. The expansion velocities and $H\alpha$ luminosities are also given in Table 1. The bright star counts are based on the OB association star counts in Lucke & Hodge (1970); again, Table 1 lists the OB associations encompassed by each superbubble. Although the scatter level of these plots is obviously high, we have attempted to fit each plot with a linear trend line to test for correlations between X-ray luminosity and other superbubble properties. The correlation coefficients of the trends are detailed in Table 6. Positive correlations are found between X-ray luminosity and each of the other properties. The correlations are moderate for the X-ray luminosities as determined by the "best-fit $N_{\rm H}$ " model fits and generally stronger for the X-ray luminosities as determined by the "fixed $N_{\rm H}$ " model fits. The strongest correlation is between "fixed $N_{\rm H}$ " X-ray luminosity and bright star count. It must be considered, however, that the correlation between X-ray luminosity and superbubble volume may be due to a surface brightness selection effect.

The correlations demonstrate that the X-ray luminosity of a superbubble is affected by the richness and age of the OB associations within its shell walls. The bright star count of a superbubble will obviously be directly related to the richness of its OB associations. Also, OB association richness will provide stellar winds to power the expansion, and thereby increase the expansion velocity, of the superbubble. The H α luminosity of a superbubble will be positively affected by the richness of OB association, as more stars provide more ionizing flux, and negatively affected by age, as the powerfully-ionizing, early-type stars exhaust themselves. The X-ray luminosity—OB association richness relationship has already been demonstrated; however, the X-ray luminosity can increase with the age of a superbubble. As demonstrated by Paper I and Wang & Helfand (1991), the X-ray luminosity of a superbubble can be enhanced by SNRs. Thus, a superbubble that has already had several bright stars go supernova can be brighter in X-rays than a superbubble with much younger OB associations. We would therefore expect the correlation between X-ray luminosity and H α luminosity to be weaker than the correlation between X-ray luminosity and bright star count, which it is

for the "fixed $N_{\rm H}$ " model fits.

4.4. Stellar Sources and Breakout Regions

We have described the X-ray morphology for each superbubble and compared those morphologies to the H α morphologies and known stellar sources of each superbubble. We have found that in a significant fraction of the superbubbles, peaks in the X-ray emission are coincident with known stellar sources, such as Wolf-Rayet stars. High-resolution observations are need to determine whether the X-ray peaks are caused by stellar emission or stellar wind interactions with the superbubble interior gas. In addition, nearly half of the superbubbles show some evidence of breakout regions in their X-ray morphologies, where hot gas appears to be leaking from the superbubble interior into the surrounding regions. Again, further studies of the diffuse X-ray gas will be needed to confirm whether these regions are true breakout regions.

5. Summary

We have presented ROSAT observation of thirteen LMC superbubbles. Eleven of these observations had not been reported previously. In each of these superbubbles, diffuse X-ray emission brighter than is theoretically expected for a wind-blown bubble was detected. Based on the previous findings in Paper I and Wang & Helfand (1991), it is reasonable to conclude that the X-ray emission from the superbubbles has been enhanced by interactions between the superbubble shell and interior SNRs. We have also found significant positive correlations between the X-ray luminosity of a superbubble and its $H\alpha$ luminosity, expansion velocity and OB star count. Further, we have found that a large fraction of the superbubbles in the sample show evidence of breakout regions. In Paper IV it was demonstrated that breakout regions can significantly affect the evolution of a superbubble, draining energy and pressure that would otherwise go into expansion. We also suggest that because these breakout regions appear so frequently, the superbubbles may be a significant source of hot gas for the interstellar medium.

We would like to thank Robert Gruendl for his useful communications in preparing this paper. This research has made use of data obtained through the High Energy Astrophysics Science Archive Research Center Online Service, provided by the NASA/Goddard Space Flight Center. This research was made possible by ADP grants NAG 5-7003 and NAG 5-8003.

REFERENCES

Arabadjis, J.S., & Bregman, J.N. 1999, ApJ, 510, 806

Bica, E.L.D., Schmitt, H.R., Dutra, C.M., Oliveira, H.L. 1998, AJ, 117, 238

Breysacher, J. 1981, A&AS, 43, 203

Chu, Y.-H., & Lasker, B.M. 1980, PASP, 92, 730

Chu, Y.-H., & Mac Low, M.-M. 1990, ApJ, 365, 510 (Paper I)

Chu, Y.-H., Mac Low, M.-M., Garcia-Segura, G., Wakker, B., Kennicutt, R.C. 1993, ApJ, 414, 213 (Paper II)

Chu, Y.-H., Chang, H.-W., Su, Y.-L., & Mac Low, M.-M. 1995, ApJ, 450, 157 (Paper III)

Chu, Y.-H., Kennicutt, R.C., Snowden, S.L., Smith, R.C., Williams, R.M., & Bomans, D.J. 1997 PASP, 109, 554

Chu, Y.-H., Weis, K., & Garnett, D.R. 1999, AJ, 117, 1433

Chu, Y.-H., Kim, S., Points, S.D., Petre, R., & Snowden, S.L. 2000, AJ, 119, 2242

Chu, Y.-H. et al. 2001, in preparation

Cowley, A.P., Schmidtke, P.C., McGrath, T.K., Ponder, A.L., & Fertig, M.R. 1997, PASP, 109, 21

Davies, R.D., Elliott, K.H., & Meaburn J. 1976, MmRAS, 81, 89

Dickey, J.M., & Lockman, F.J. 1990, ARAA, 28, 215

Feast, M. 1999, PASP, 111, 775

Georgelin, Y.M., Georgelin, Y.P., Laval, A., Monnet, G., Rosado, M. 1983, A&AS, 54, 459

Hail, T.C., Dunne, B.C, & Chu, Y.-H. 2001, in preparation

Henize, K.G. 1956, ApJS, 2, 315

Hodge, P.W., & Sexton, J.A. 1966, AJ, 71, 363

Kennicutt, R.C., & Hodge, P.W. 1986, ApJ, 306, 130

Lucke, P.B., & Hodge P.W. 1970, AJ, 75, 171

Mac Low, M.-M., Chang, T.H., Chu, Y.-H., Points, S.D., Smith, R.C., Wakker, B.P. 1998, AJ, 493, 260 (Paper V)

Mathewson, D.S., Ford, V.L., Dopita, M.A., Tuohy, I.R., & Long, K.S. 1983, ApJS, 51, 345

Mathewson, D.S., Ford, V.L., Tuohy, I.R., Mills, B.Y., Turtle, A.J., & Helfand, D.J. 1985, ApJS, 58, 197

Magnier, E.A, Chu Y.-H., Points, S.D., Hwang, U., Smith, R.C. 1996, ApJ, 464, 829 (Paper IV)

Meaburn, J., & Laspias, N.V. 1991, A&A, 245, 635

Morrison, R., & McCammon, D. 1983, ApJ, 270, 119

Oey, M.S., & Smedley, S.A. 1998, AJ, 116, 1263

Osterberg, J. 1997, private communication

Points, S.D., Chu, Y.-H., Kim, S., Smith, R.C., Snowden, S.L., Brandner, W., Greundl, R.A. 1999, ApJ, 518, 298

Pfefferman, E., et al. 1987, Proc. SPIE, 733, 519

Raymond, J.C., & Smith, B.W. 1977, ApJS, 35, 419

Rohlfs, K., Kreitschmann, J., Feitzinger, J.V., Siegman, B.C. 1984, A&A, 137, 343

Rosado, M., Laval, A., Le Coarer, E., Georgelin, Y.P., Amram, P., Marcelin, M., Goldes, G., & Gach, J.L. 1996, A&A, 308, 588

ROSAT Mission Description, 1991, NASA publication NRA 91-OSSA-25, Appendix F

Sanduleak, N. 1969, Cerro Tololo Inter-American Obs. Contrib. No. 89

Wang, Q., & Helfand, D.J. 1991, ApJ, 373, 497

Weaver, R., McCray, R., Castor, J., Shapiro, P., & Moore, R. 1977, ApJ, 208, 610

Williams, R.M., Chu, Y.-H., Dickel, J.R., Petre, R., Smith, R.C., & Tavarez, M. 1999, ApJS, 123, 467

Williams, R.M., Petre, R., Chu, Y.-H., Chen, C.H.R. 2000, ApJ, 536, 27

Willis, A. J. 1999, in: K.A. van der Hucht, G. Koenigsberger, & P.R.J. Eenens (eds.), Wolf-Rayet Phenomena in Massive Star and Starburst Galaxies, Proc. IAU Symp. No. 193 (Chelsea, Mich: Sheridan)

This preprint was prepared with the AAS LATEX macros v5.0.

- Fig. 1.— For each pair, the left image show H α emission from the superbubble(s) overlaid with X-ray contours. The right image, shows the X-ray emission overlaid with the same contours to ensure the clarity of the contour levels. The contours are at levels of 50%, 70%, 85%, and 95% of the peak level within the superbubble. For bright X-ray objects in the field not actually part of the superbubble (such as SNRs), we have plotted additional contours at 2, 4, 8, and 16 times the superbubble peak level. These contours are plotted as dashed lines. Locations of the superbubbles are indicated in the H α images. (a) N11–Shell 1; (b) N44; (c) N51; (d) N57; (e) N103; (f) N105; (g) N144; (h) N154; (i) N158; (j) N160; (k) N206; and (l) 30 Dor C.
- Fig. 2.— Each plot shows the superbubble's X-ray spectra and the "best-fit $N_{\rm H}$ " spectral fit. (a) N11–Shell 1; (b) N44; (c) N51–DEM L 192; (d) N51–DEM L 205. (e) N57; (f) N103; (g) N105; (h) N144; (i) N154; (j) N158; (k) N160; (l) N206. (m) 30 Dor C–east side; (n) 30 Dor C–west side;
- Fig. 3.— Each plot shows the superbubble's X-ray spectra and the "fixed $N_{\rm H}$ " spectral fit. (a) N11–Shell 1; (b) N44; (c) N51–DEM L 192; (d) N51–DEM L 205. (e) N57; (f) N103; (g) N105; (h) N144; (i) N154; (j) N158; (k) N160; (l) N206. (m) 30 Dor C–east side; (n) 30 Dor C–west side;
- Fig. 4.— Superbubble X-ray luminosity distribution. X-ray luminosity is plotted on a logarithmic scale. The 0.2 bin size was used.
- Fig. 5.— Superbubble X-ray luminosity vs. volume for the "best-fit $N_{\rm H}$ " X-ray spectral fits (upper) and "fixed $N_{\rm H}$ " X-ray spectral fits (lower). Luminosity is plotted on a logarithmic scale. The volumes are based on H α morphology. A linear trend line is plotted for each graph.
- Fig. 6.— Superbubble X-ray luminosity vs. $H\alpha$ luminosity for the "best-fit $N_{\rm H}$ " X-ray spectral fits (upper) and "fixed $N_{\rm H}$ " X-ray spectral fits (lower). Both luminosities are plotted on a logarithmic scale. A linear trend line is plotted for each graph.
- Fig. 7.— Superbubble X-ray luminosity vs. $H\alpha$ expansion velocity for the "best-fit $N_{\rm H}$ " X-ray spectral fits (upper) and "fixed $N_{\rm H}$ " X-ray spectral fits (lower). Luminosity is plotted on a logarithmic scale. A linear trend line is plotted for each graph.
- Fig. 8.— Superbubble X-ray luminosity vs. bright star count for the "best-fit $N_{\rm H}$ " X-ray spectral fits (upper) and "fixed $N_{\rm H}$ " X-ray spectral fits (lower). Luminosity is plotted on a logarithmic scale. Bright star counts are based on star counts in local OB associations (Lucke & Hodge 1970).

Table 1. LMC Superbubble Properties

Object ^a	DEM No.b	Local OB ^c Associations	α_{2000} (h:m:s)	$\delta_{2000} \ (\circ : : ")$	$\begin{array}{c} \rm Size^d \\ (pc \times pc) \end{array}$	$\log L_{\rm H\alpha}{}^{\rm d}$ (ergs sec ⁻¹)	Expansion Velocity (km sec^{-1})
N11–Shell 1	DEM L 34	LH 9	04:56:51	-66:24:24	150×100	36.90	$45^{\rm e}$
N44	$\mathrm{DEM} \ \mathrm{L} \ 152$	LH 47	05:22:08	-67:56:12	100×75	37.00	40^{f}
N51	$\mathrm{DEM} \; \mathrm{L} \; 192$	LH 51, LH 54	05:26:14	-67:30:18	135×120	37.04	$20 – 50^{g}$
	$\mathrm{DEM} \ \mathrm{L} \ 205$	LH 63	05:28:06	-67:28:36	65×50	36.26	$45 - 70^{g}$
N57	$\mathrm{DEM} \ \mathrm{L} \ 229$	LH 76	05:32:24	-67:41:18	135×105	36.91	${\sim}45^{\rm g}$
N103B	DEM L 84	NGC1850	05:08:54	-68:45:00	120×120	36.53	$20^{\rm h}$
N105	DEM L 86	LH 31	05:09:57	-68:53:31	90×60	36.82	_
N144	$\mathrm{DEM} \; \mathrm{L} \; 199$	LH 58	05:26:33	-68:51:48	120×75	36.98	$20 – 30^{g}$
N154	$\mathrm{DEM} \ \mathrm{L} \ 246$	LH 81, LH 87	05:35:57	-69:38:54	180×120	37.10	_
N158	$\mathrm{DEM} \ \mathrm{L} \ 269$	LH 101, LH 104	05:39:33	-69:25:48	120×100	36.80	$\sim 45^{\mathrm{g}}$
N160	$\mathrm{DEM} \ \mathrm{L} \ 284$	LH 103	05:40:12	-69:37:06	180×150	37.22	$\lesssim 20^{\mathrm{g}}$
N206	$\mathrm{DEM} \ \mathrm{L} \ 221$	LH 66, LH 69	05:29:36	-71:00:00	90×90	36.95	$\sim 30^{\rm g}$
30 Dor C	$\mathrm{DEM} \ \mathrm{L} \ 263$	LH 90	05:38:42	-69:06:03	100×90	36.94	${\sim}45^{\rm g}$

^aNomenclature of Henize (1956), except 30 Dor C

^bNomenclature of Davies, Elliott, & Meaburn (1976)

 $^{^{\}rm c}{\rm Nomenclature}$ of Lucke & Hodge $\,$ (1970), except NGC 1850 $\,$

 $^{^{\}rm d} \rm Determined$ from PDS scans of Kennicutt & Hodge (1986), includes only ${\rm H}\alpha$ emission from the superbubble shell

^eRosado et al. (1996)

^fMeaburn & Laspias (1991)

^gChu et al. (2001)

^hGeorgelin et al. (1983)

Table 2. Archival ROSAT Observations

Field(s)	ROSAT ID	PI	α_{2000} (h:m:s)	δ_{2000} (°:':")	Exposure Time (sec)	Off-axis Angle (arcmin)
N11	rp900320a01	Chu	04:56:33.6	-66:28:48	13731	4.7
	rp900320n00	Chu	04:56:33.6	-66:28:48	17589	4.7
N44	rp400154n00	Pakull	05:22:26.4	-67:58:12	6522	2.2
	rp500093n00	Chu	05:22:02.4	-67:55:12	8720	2.2
N51, N57	rp500054a00	Fink	05:25:52.8	-67:30:00	3420	5.3, 39.7
	rp500054a01	Fink	05:25:52.8	-67:30:00	4452	5.3, 39.7
N103, N105	$\rm rp500037n00$	Aschenbach	05:08:60.0	-68:43:48	6826	1.3, 11.0
N144	rp500138a01	MacLow	05:26:36.0	-68:50:24	14531	1.4
	rp500138a02	MacLow	05:26:36.0	-68:50:24	14581	1.4
	rp500138n00	MacLow	05:26:36.0	-68:50:24	2478	1.4
N154, 30 Dor C	rp180251n00	Aschenbach	05:35:28.8	-69:16:12	20153	22.8, 13.4
	rp500100a00	Gorenstein	05:35:28.8	-69:16:12	16957	22.8, 13.4
	rp500100a01	Gorenstein	05:35:28.8	-69:16:12	9657	22.8, 13.4
	$\rm rp500140a02$	Gorenstein	05:35:28.8	-69:16:12	10758	22.8, 13.4
	$\rm rp500140n00$	Gorenstein	05:35:28.8	-69:16:12	2642	22.8, 13.4
	$\rm rp500303n00$	Hasinger	05:35:28.8	-69:16:12	9416	22.8, 13.4
N158	$\rm rp400052n00$	Oegelman	05:40:12.0	-69:19:48	8823	10.9
	rp400133n00	Oegelman	05:40:12.0	-69:19:48	1803	10.9
N160	rp400079n00	Lewin	05:39:38.4	-69:44:24	7429	7.9
N206	rp300172a01	Oegelman	05:32:28.8	-70:21:36	2993	41.0
	rp300172a02	Oegelman	05:32:28.8	-70:21:36	3880	41.0
	rp300172n00	Oegelman	05:32:28.8	-70:21:36	6272	41.0
	rh600781a01	Chu	05:30:45.6	-71:02:24	24041	6.1
	$\mathrm{rh}600781\mathrm{n}00$	Chu	05:30:45.6	-71:02:24	25238	6.1

Table 3. "Best-Fit $N_{\rm H}$ " LMC Superbubble X-ray Spectral Fits

Object	Exposure (sec)	Background Subtracted Source Counts	Scaled Background Counts	$\log N_{ m H} \ m (cm^{-2})$	kT (keV)	$\log L_{\rm X}^{\rm a}$ (erg s ⁻¹)	$N_{\rm e}\sqrt{f}$ $(10^{-2}~{\rm cm}^{-3})$
N11–Shell 1	31320	1775	1667	21.9	0.13	37.17	31.
N44	15242	2894	1260	20.6	0.71	35.73	3.8
N51							
$\mathrm{DEM}\ \mathrm{L}\ 192$	7872	559	865	20.4	0.28	35.18	1.5
$\mathrm{DEM}\ \mathrm{L}\ 205$	7872	220	226	20.5	0.25	34.86	3.7
N57	7872	398	489	20.6	0.33	35.32	1.8
N103B	6826	99	120	21.3	0.72	34.85	0.8
N105	6826	158	183	21.6	0.31	35.40	4.6
N144	31590	667	1399	20.5	0.32	34.74	1.3
N154	81210	6269	9618	20.7	0.29	35.52	1.8
N158	10626	2543	1236	20.7	0.60	35.85	3.0
N160	7429	964	1517	20.9	3.40	35.80	1.9
N206	13145	330	490	20.7	0.31	35.09	2.2
30 Dor C							
East	81210	5378	4388	21.1	1.19	35.49	4.0
West	81210	1887	3225	22.0	1.22	35.84	7.4

 $^{^{\}rm a}{\rm In}$ the energy band 0.5–2.4 keV.

Table 4. "Fixed $N_{\rm H}$ " LMC Superbubble X-ray Spectral Fits

Object	$\log (N_{\rm HI})_{\rm Galactic}^{\rm a}$ $({\rm cm}^{-2})$	$\frac{\log (N_{\rm HI})_{\rm LMC}^{\rm b}}{({\rm cm}^{-2})}$	$\log N_{\rm H}$ $(\rm cm^{-2})$	kT (keV)	$\log L_{\rm X}^{\rm c}$ (erg s ⁻¹)	$N_{\rm e}\sqrt{f}$ $(10^{-2}~{\rm cm}^{-3})$
N11–Shell 1	20.63	21.45	21.6	0.24	35.96	4.2
N44	20.79	21.45	21.6	0.35	36.36	9.3
N51						
DEM L 192	20.78	21.07	21.4	0.18	35.82	4.1
$\mathrm{DEM}\ \mathrm{L}\ 205$	20.77	20.89	21.3	0.18	35.37	8.2
N57	20.78	21.23	21.5	0.23	35.91	4.3
N103B	20.79	21.30	21.5	0.65	35.02	1.0
N105	20.81	21.30	21.5	0.34	35.28	3.5
N144	20.79	20.87	21.3	0.25	35.12	2.3
N154	20.82	21.58	21.7	0.15	36.88	14.
N158	20.83	21.52	21.7	0.28	36.66	10.
N160	20.84	21.53	21.7	0.93	36.07	2.4
N206	20.84	21.27	21.5	0.20	35.80	6.1
30 Dor C						
East	20.81	21.63	21.7	0.79	35.90	5.4
West	20.81	21.63	21.7	_d	35.54	5.1

 $^{^{\}mathrm{a}}\mathrm{Dickey}~\&~\mathrm{Lockman}~~(1990)$

^bRohlfs et al. (1984)

 $^{^{\}rm c}{\rm In}$ the energy band 0.5–2.4 keV.

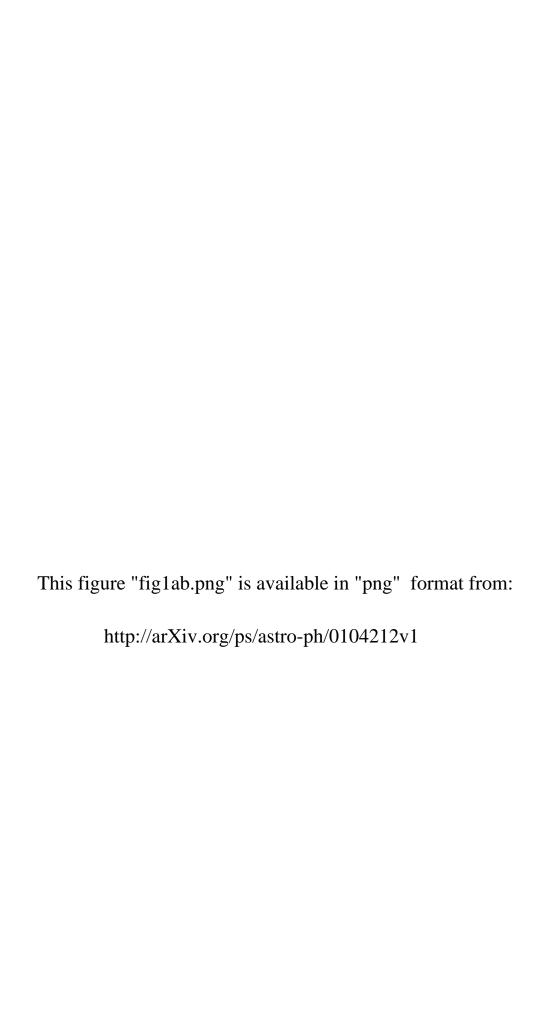
 $^{^{\}rm d}$ Unable to Find Solution

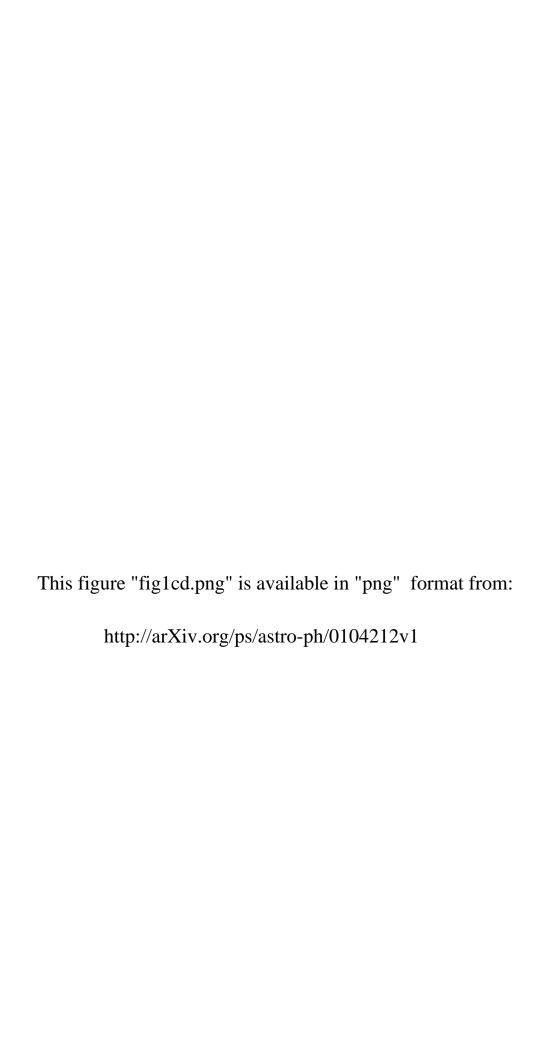
Table 5. Superbubble Emission Measures and Pressure-Driven Model X-Ray Luminosities

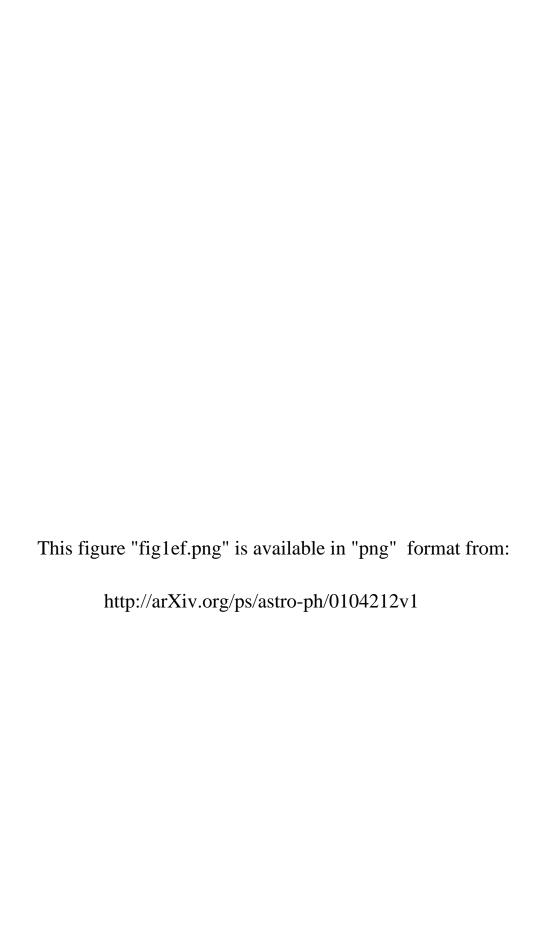
Object	Mean Emission Measure $(cm^{-6} pc)$	$\begin{array}{c} \text{Size} \\ (\text{pc} \times \text{pc}) \end{array}$	Expansion Velocity (km sec^{-1})	$\log (L_{ m X})_{ m Model}$ (erg sec ⁻¹)	$\log (L_{\rm X})_{\rm Best-Fit}$ (erg sec ⁻¹)	$\log (L_{\rm X})_{\rm Fixed}$ $({\rm erg~sec}^{-1})$
N11-Shell 1	~750	150×100	45	34.8	37.17	35.96
N44	~ 3000	100×75	40	35.1	35.73	36.36
N51						
DEM L 192	~ 1750	135×120	20 – 50	34.8	35.18	35.82
$\mathrm{DEM} \ \mathrm{L} \ 205$	~ 1200	65×50	45 - 70	35.1	34.86	35.37
N57	~ 1500	135×105	~ 45	35.0	35.32	35.91
N103B	~ 1000	120×120	20	34.2	34.85	35.02
N144	~ 1500	120×75	20 – 30	34.5	34.74	35.12
N158	~ 2000	120×100	~ 45	35.0	35.85	36.66
N160	~ 1250	180×150	$\lesssim 20$	34.3	35.80	36.07
N206	~ 1500	90×90	~ 30	34.6	35.09	35.80
30 Dor C	~ 2000	100×90	$\sim \! 45$	35.0	36.00	36.06

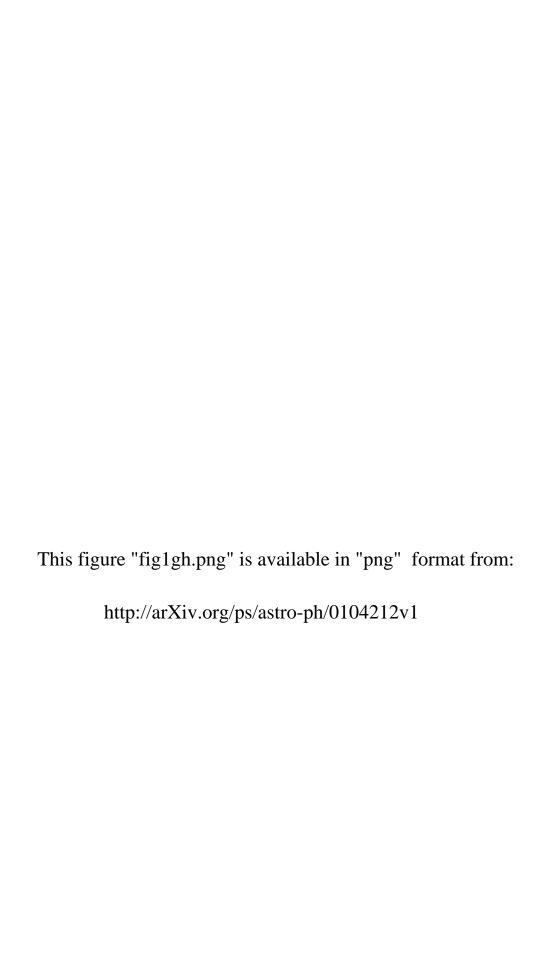
Table 6. Correlation Coefficients

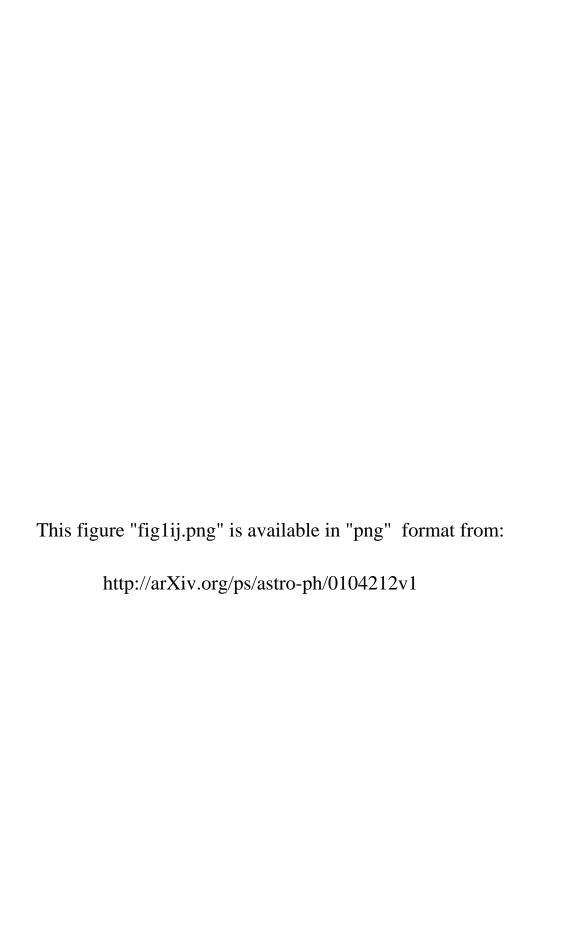
$Plot \ L_{ m X} \ { m vs.}$	Correlation C Best-Fit $N_{\rm H}$	
Superbubble Volume	0.30	0.40
$H\alpha$ Luminosity	0.33	0.51
Expansion Velocity	0.26	0.31
Bright Star Count	0.35	0.83

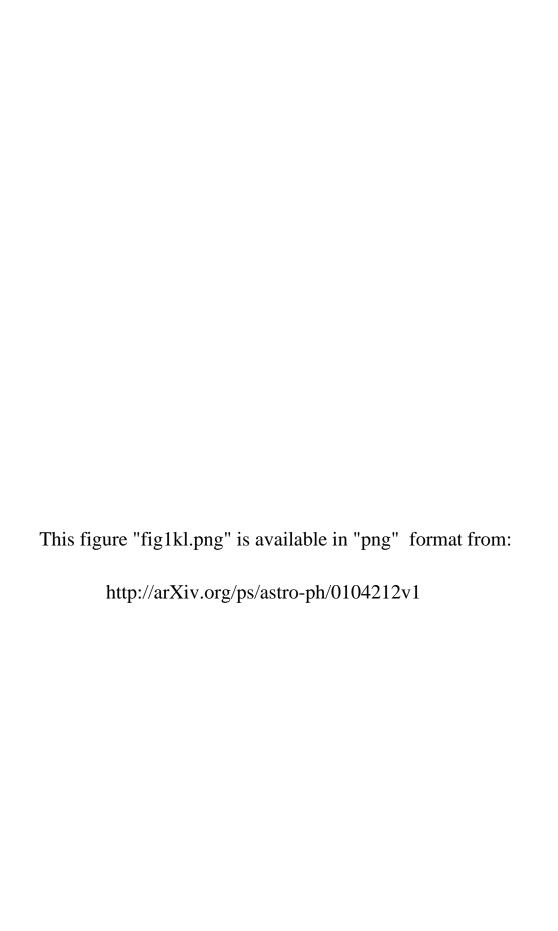












This figure "fig2.png" is available in "png" format from:

This figure "fig3.png" is available in "png" format from:

This figure "fig4.png" is available in "png" format from:

This figure "fig5.png" is available in "png" format from:

This figure "fig6.png" is available in "png" format from:

This figure "fig7.png" is available in "png" format from:

This figure "fig8.png" is available in "png" format from: